The Astrophysical Journal, 935:173 (13pp), 2022 August 20 https://doi.org/10.3847/1538-4357/ac8101

The Solar Minimum Eclipse of 2019 July 2. II. The First Absolute Brightness Measurements and MHD Model Predictions of Fe X, XI, and XIV out to 3.4 $R_\odot$

Benjamin Boe[1], Shadia Habbal[1], Cooper Downs[2], and Miloslav Druckmüller[3]
[1] Institute for Astronomy, University of Hawaii, Honolulu, HI 96822, USA; bboe@hawaii.edu
[2] Predictive Science Inc., San Diego, CA 92121, USA
[3] Faculty of Mechanical Engineering, Brno University of Technology, Technicka 2, 616 69 Brno, Czech Republic
Received 2022 June 7; revised 2022 July 5; accepted 2022 July 12; published 2022 August 24

Abstract

We present the spatially resolved absolute brightness of the Fe X, Fe XI, and Fe XIV visible coronal emission lines from 1.08 to 3.4 $R_\odot$, observed during the 2019 July 2 total solar eclipse (TSE). The morphology of the corona was typical of solar minimum, with a dipole field dominance showcased by large polar coronal holes and a broad equatorial streamer belt. The Fe XI line is found to be the brightest, followed by Fe X and Fe XIV (in disk $B_\odot$ units). All lines had brightness variations between streamers and coronal holes, where Fe XIV exhibited the largest variation. However, Fe X remained surprisingly uniform with latitude. The Fe line brightnesses are used to infer the relative ionic abundances and line-of-sight-averaged electron temperature (T_e) throughout the corona, yielding values from 1.25 to 1.4 MK in coronal holes and up to 1.65 MK in the core of streamers. The line brightnesses and inferred T_e values are then quantitatively compared to the Predictive Science Inc. magnetohydrodynamic model prediction for this TSE. The MHD model predicted the Fe lines rather well in general, while the forward-modeled line ratios slightly underestimated the observationally inferred T_e within 5%–10% averaged over the entire corona. Larger discrepancies in the polar coronal holes may point to insufficient heating and/or other limitations in the approach. These comparisons highlight the importance of TSE observations for constraining models of the corona and solar wind formation.

Unified Astronomy Thesaurus concepts: Solar corona (1483); Solar eclipses (1489); Solar coronal streamers (1486); Solar cycle (1487); Solar coronal holes (1484); Solar optical telescopes (1514)

1. Introduction

Coronal emission lines were first discovered and identified in the visible and near-infrared during total solar eclipses (TSEs) in the late 19th (Young 1872) and early 20th centuries (Lyot 1939). Subsequent observations focused on the so-called "green" (Fe XIV, 530.3 nm) and "red" (Fe X, 637.4 nm) lines (e.g., Magnant-Crifo 1973; Chandrasekhar et al. 1984; Bessey & Liebenberg 1984; Guhathakurta et al. 1992). The observed emission was typically limited to a helioprojective distance less than 1.4 $R_\odot$, though occasionally emission was recorded up to 1.7 $R_\odot$ (Singh et al. 1982). Recent work has continued to employ line emission observed during TSEs as a means to study the physical properties of the solar corona, including the ionic freeze-in distances (Habbal et al. 2007, 2013; Boe et al. 2018), the average electron temperature (T_e; Boe et al. 2020a), the sources of the solar wind in the corona (Habbal et al. 2021), and the presence of various ionic species with slit spectrographs (Ding & Habbal 2017; Samra et al. 2018; Koutchmy et al. 2019).

Given the diagnostic potential of coronal emission lines, and the relative sparsity of TSEs, coronagraphs have often been utilized to study coronal line emission. Lyot (1932) was the first to use a coronagraph to simulate a TSE, and was followed by systematic observations of Fe XIV in the very low corona (≈1.15 $R_\odot$) over several decades (Rybansky et al. 1994; Altrock 2011). More recent observations have utilized the near-infrared Fe XIII (1074.4 nm) line (e.g., Dima et al. 2019; Rumińska et al. 2022), especially to measure the coronal magnetic field. In the near future, additional observations of numerous coronal visible lines will be performed with the ground-based UCoMP instrument (Tomczyk et al. 2021).

Space-based coronagraphs have also been utilized to study visible lines to some extent, including measurements of the line brightness (Wang et al. 1997; Srivastava et al. 2000) and line widths (Mierla et al. 2008) of both Fe XIV and Fe X with the LASCO-C1 instrument in the low corona ($\lessapprox$1.5 $R_\odot$). Unfortunately, these observations were not absolutely calibrated and the data from C1 were limited due to its failure early in the Solar and Heliospheric Observatory (SOHO) mission. Consequently, observations of coronal lines at visible wavelengths have been rather limited except during TSEs and have been limited in spatial extent to 1.7 $R_\odot$ at most. (See Del Zanna & DeLuca 2018 for a detailed historical overview of observations of visible and near-infrared coronal line emission.)

In this work, we analyze observations of the Fe X, Fe XI, and Fe XIV emission lines from the 2019 July 2 TSE. The observation and calibration procedures are discussed in Section 2. In Section 3.1 we discuss the spatially resolved absolute brightness of each emission line throughout the corona from 1.08 to 3.4 $R_\odot$. In Section 3.2 we infer the spatially resolved line-of-sight (LOS) averaged electron temperature T_e via the Fe line ratios. Finally, in Section 4 we compare the line emission and T_e values to the predictions of the Predictive Science Inc. (PSI) magnetohydrodynamic (MHD) simulation of this eclipse. A discussion and summary of the results is given in Section 5.

2. 2019 Total Solar Eclipse Observations

The eclipse observations used in this work were acquired during the 2019 July 2 total solar eclipse over Rodeo,

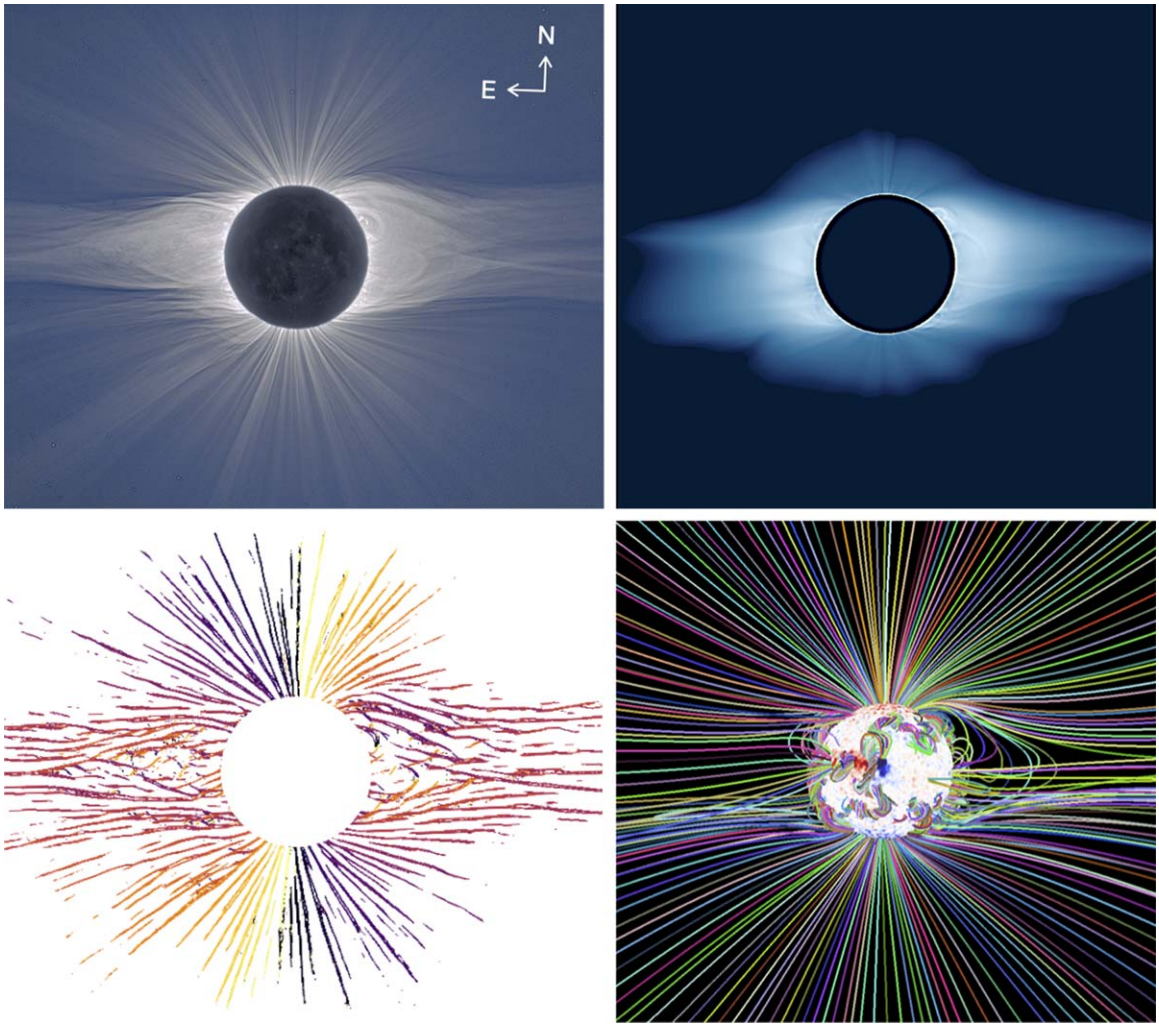

Figure 1. Top left: high-spatial-resolution white-light image of the eclipse corona, with terrestrial north pointing upward. The compass indicates solar north, which is two degrees clockwise of terrestrial north. Top right: PSI MHD model prediction of the white-light corona (see Section 4), with the same orientation and scale as the eclipse image to the left. Bottom left: quantitative trace of the magnetic field morphology during the eclipse, made with the white-light image, previously presented in Boe et al. (2020b). Bottom right: traces of the coronal magnetic field lines from the PSI MHD model prediction of the eclipse, aligned to the white-light image.

Argentina, where totality lasted 2 minutes and 14 s. The high-spatial-resolution broadband white-light image in the top left panel of Figure 1 highlights the magnetic morphology of solar minimum with a dipolar field dominance. Specifically, the corona consisted of large polar coronal holes dominated by open magnetic field lines and a wide streamer belt centered on the solar equator. The fine-scale magnetic morphology inferred from the white-light image is showcased by the quantified topological map in the bottom left panel of Figure 1 (previously presented in Boe et al. 2020b). Further, there were not any coronal mass ejections (CMEs) or flares of any kind reported on the day of the eclipse by the Space Weather Database of Notification, Knowledge, Information (DONKI).[4] Hence the corona on this day is an excellent example of a minimally perturbed corona. However, just because the Sun was at solar minimum does not inherently preclude the occurrence of a CME perturbing the corona. Indeed, Boe et al. (2020c) found a large CME in the corona during the 2020 TSE, which occurred less than 18 months after the 2019 TSE presented here; that CME demonstrated large-scale dynamical interactions between an active-region CME and a nearby streamer.

[4] https://ccmc.gsfc.nasa.gov/donki/

In addition to the white-light data, we present observations of the Fe X (637.4 nm), Fe XI (789.2 nm), and Fe XIV (530.3 nm) emission lines. In the top panels of Figure 2, we show processed versions of the Fe X, Fe XI, and Fe XIV line emission, where the radial brightness gradient has been removed to highlight small-scale spatial variations (see Druckmüller et al. 2006).

The line emission data were acquired with narrowband imaging systems that had bandpasses of ≈0.5 nm, which we refer to as "on-band." For each emission line observation, we make an additional continuum observation with an identical telescope system, but with its bandpass shifted 1–3 nm toward the blue of the emission line, which were refer to as "off-band." The bandpasses for all emission lines (i.e., on-band) and corresponding continuum observations (i.e., off-band) are shown in Figure 3. The bandpass curves are from the transmission of the filters measured by the manufacturer (Andover Corporation). Similar imaging systems have also been used at many previous eclipses (see Habbal et al. 2010a, 2013, 2014, 2021; Boe et al. 2018, 2020a). Details of these telescopic systems and observational methodology for this eclipse specifically were discussed at length in Boe et al. (2021a), where the set of off-band observations across the

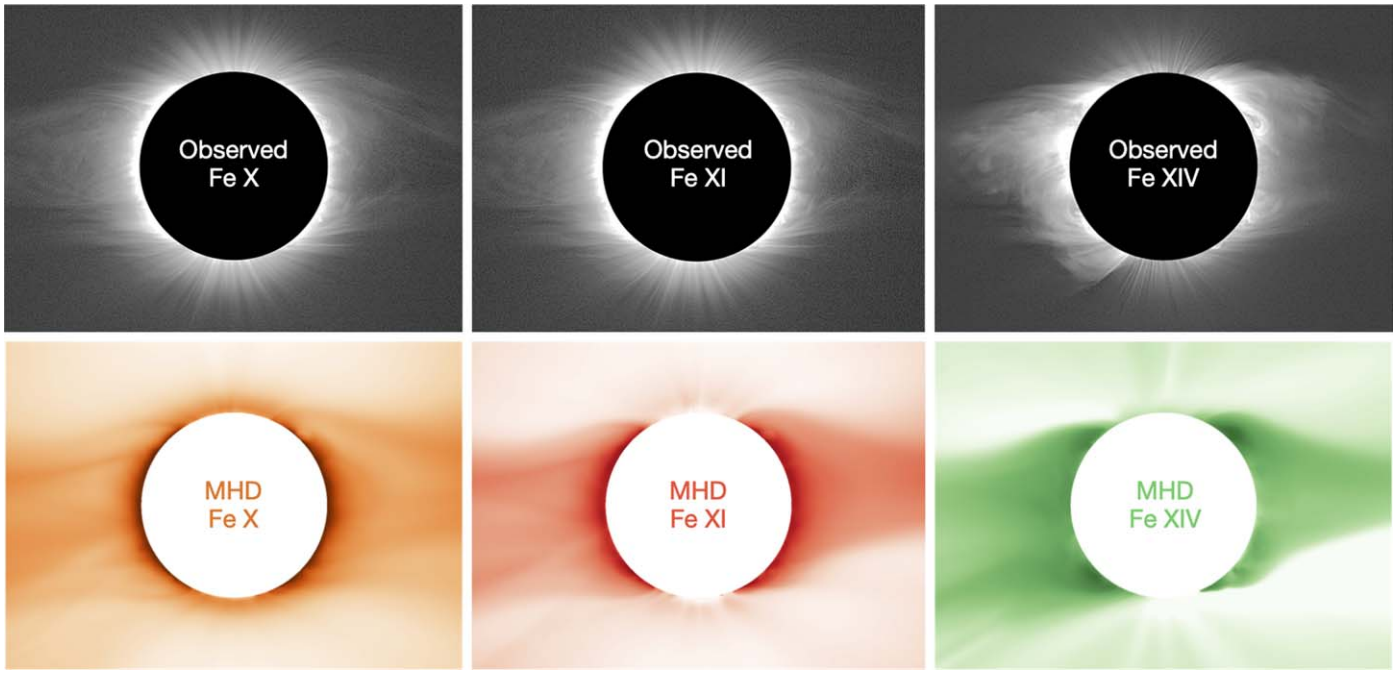

Figure 2. Top: images of Fe X, Fe XI, and Fe XIV line emission (see Habbal et al. 2021), with solar north upward. All images have been processed to remove the radial gradient in brightness and enhance the fine-scale structures. Bottom: prediction of emission from the same lines as above from the PSI MHD model. These images have been radially flattened and are shown on a logarithmic scale to enhance fine-scale details in the emission (analogous to the top panels).

visible spectrum were used to isolate the K- and F-corona using a color-based inversion technique.

These emission line observations allow us to probe coronal plasmas at different T_e spanning the expected range of values from 0.8 to 2.5 MK, given the ionic abundance curves shown in the top panel of Figure 4, which are taken from version 10 of the CHIANTI database (Dere et al. 1997; Del Zanna et al. 2021). These ionic equilibrium data have been interpolated from their recorded spacing of $\Delta\log(K) = 0.05$ into the smooth curves shown in the figure.

2.1. Data Calibration

Since the continuum data were already calibrated into solar disk brightness units ($B_\odot$, see Boe et al. 2021a), via the Mauna Loa Solar Observatory's (MLSO) K-coronagraph (K-Cor),[5] we used the off-band to calibrate the on-band data. First, we measured the sky brightness at the center of the Moon during totality in each composite eclipse image (both on- and off-band) and subtracted it to set the correct zero-point. Next, we took the pixel flux in a region in the corner of each on- and off-band image $>3.5\,R_\odot$, and set them equal to each other in each image pair. In doing so, we assumed that the line emission is negligible at that distance given the dominance of the F-corona emission over both the K-corona and line emission (see Boe et al. 2021a). Any remaining K-corona at that distance would further wash out the presence of negligible line emission. Once the on- and off-band pairs had been self-calibrated, we added back the expected earthshine brightness on the Moon of $2.5 \times 10^{-10} \pm 1.5 \times 10^{-10} B_\odot$ (Agrawal 2016). Once the data were transformed into solar disk brightness units, the continuum (off-band) images were subtracted from the on-band data to isolate the brightness of each emission line.

[5] K-Cor doi:10.5065/D69G5JV8; https://mlso.hao.ucar.edu/mlso_data_calendar.php.

2.2. Line Width Correction

Finally, we performed a correction to the line emission data based on the expected line widths and known bandpasses. The bandpasses were designed to be broader than the line widths, but the bandpasses are not a perfect boxcar function (see Figure 3), so we had to account for the effect that the shape of the bandpass had on the final integrated line brightness.

To determine the expected line widths, we used the expected effective ion temperatures ($T_{\rm eff}$). $T_{\rm eff}$ is a measure directly determined by the line width according to the following equation:

$$T_{\rm eff}^i = \frac{m_i}{2k}\Delta\lambda^2\left(\frac{c}{\lambda}\right)^2, \quad (1)$$

where m_i is the mass of the ion, k is Boltzmann's constant, c is the speed of light, λ is the line wavelength, and $\Delta\lambda$ is the Doppler width, defined by the standard deviation of the Gaussian line (i.e., σ). Note that the FWHM is 2.355σ for a Gaussian function. Equation (1) and an estimate of $T_{\rm eff}$ then allow one to determine the expected width for an arbitrary line. $T_{\rm eff}$ is related to the ion temperature, with additional broadening due to turbulent and nonthermal motions. Since we only need an estimate of the line width, and not the actual ion temperature, $T_{\rm eff}$ is sufficient for our purposes.

For our estimate of $T_{\rm eff}$ throughout the corona, we used a number of previously published estimates. We used UVCS/SOHO measurements of $T_{\rm eff}$ of the Mg X 62.6 nm and O VI 103.7 nm lines, as reported by Esser et al. (1999), which probed helioprojective distances beyond $2.2\,R_\odot$. For shorter helioprojective distances, we used line width observations from the LASCO-C1 coronagraph of Fe XIV 530.3 nm (Mierla et al. 2008), which we converted to $T_{\rm eff}$ using Equation (1). We also used EUV observations from EIS/Hinode observations, reported as the effective ion velocity (i.e., $v_{\rm eff} = c\Delta\lambda/\lambda$) of

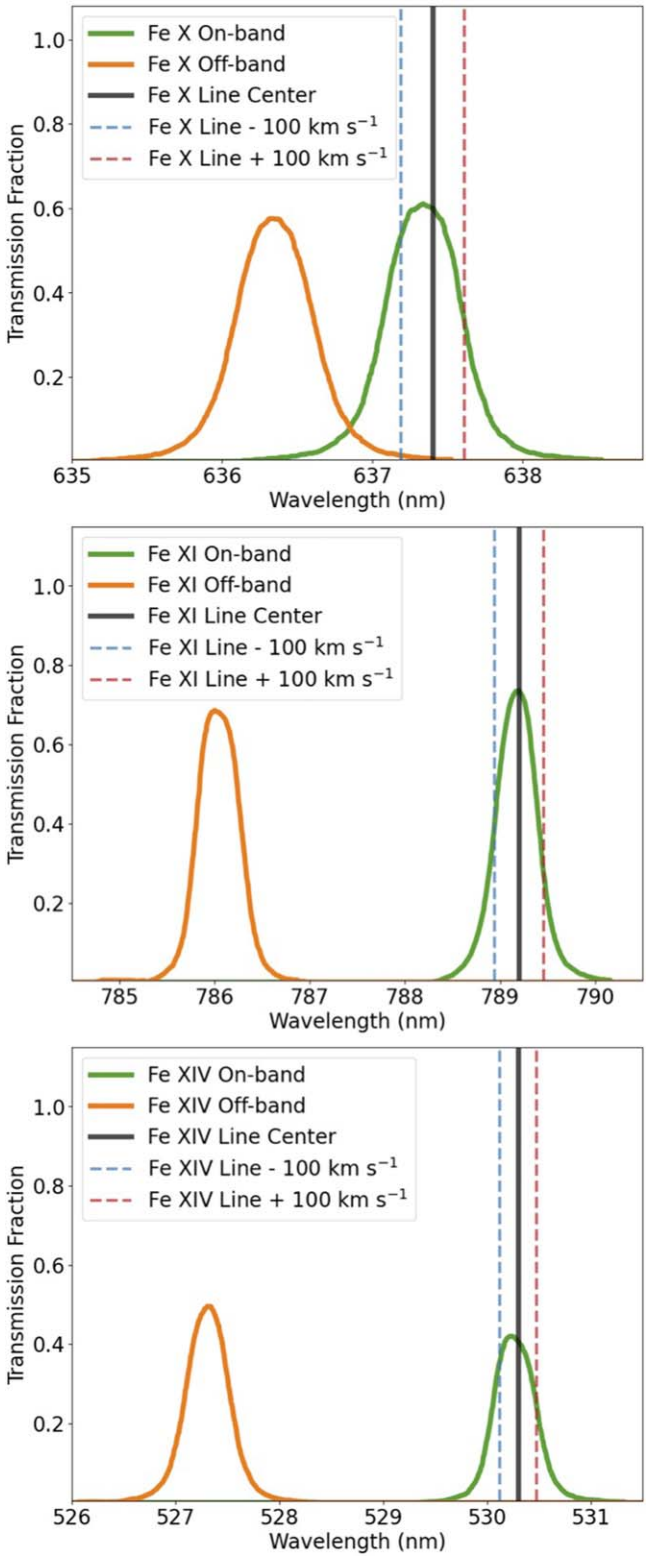

Figure 3. The set of narrowband filter profiles for the line (on-band) and continuum (off-band) of Fe X, Fe XI, and Fe XIV, as measured by the manufacturer. The bandpasses are indicated by green curves for the on-band and by orange curves for the off-band, which are shifted to slightly lower wavelengths than the line emission. Each line center is denoted by a vertical black line along with dashed blue- and redshifted locations at 100 km s^{-1} (which is faster than expected for Doppler velocities in the corona).

the Fe XI 18.8 nm line (Hahn & Savin 2013). We then fit an exponential function to this set of data using Scipy `curve_fit` (as shown in the top panel of Figure 5), which

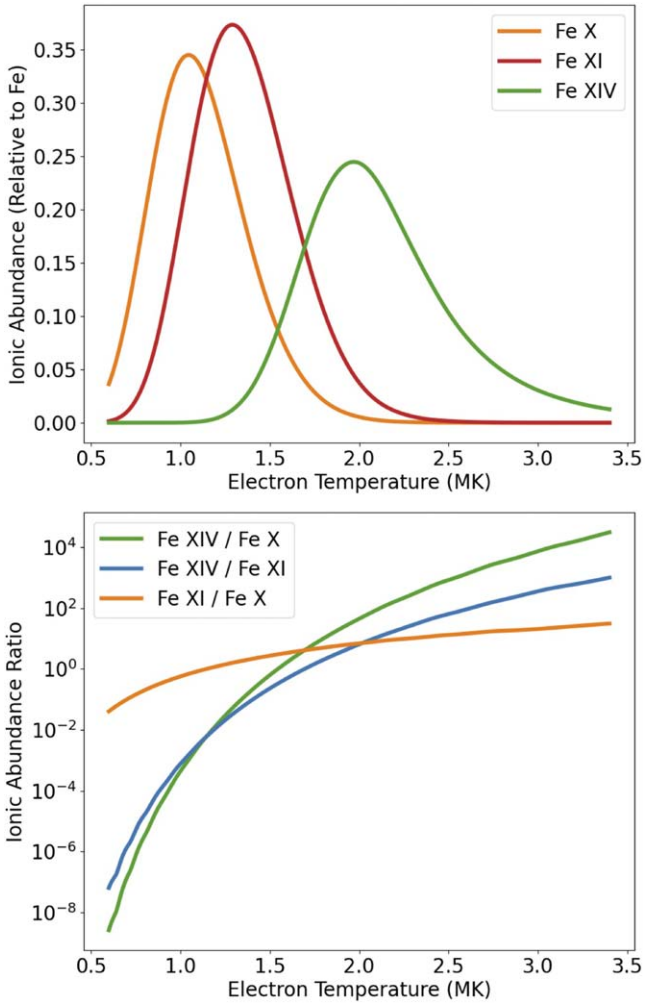

Figure 4. Top: ionic abundances versus T_e with values interpolated from CHIANTI for Fe X, Fe XI ,and Fe XIV. Bottom: ionic abundance ratios from the ionic abundance curves above versus T_e.

gave $T_{\rm eff} = (0.13 \pm 0.01)e^{(2.03 \pm 0.08)R}$, with R given in units of $R_\odot$, and $T_{\rm eff}$ in MK. With the fit to $T_{\rm eff}$, we computed the expected FWHM for each observed emission line, as shown in the middle panel of Figure 5.

To determine the correction factor needed for each line, we had to determine the relative transmission of the line and continuum signals integrated over the bandpasses. The line transmission efficiency was determined as the integrated product of a Gaussian function of the expected line width with the known bandpass for each line. The efficiency of transmitting the K + F corona signal, the integral of which was calibrated to the solar disk brightness (see Section 2.1), was found by integrating a flat continuum source over the bandpass since the K + F corona continuum is effectively flat over the narrow bandpasses. The ratio of these integrals gives the correction factor for each line, C_i, written as

$$C_i = \frac{\int b_i(\lambda)\, d\lambda}{\int G_i(\lambda, \Delta\lambda)\, b_i(\lambda)\, d\lambda} \quad (2)$$

where b_i is the bandpass transmission function (see Figure 3) for line i with a Gaussian line profile G_i defined by the line width $\Delta\lambda$, which will vary with helioprojective distance. This correction factor accounts for the relative transmission of the bandpasses and

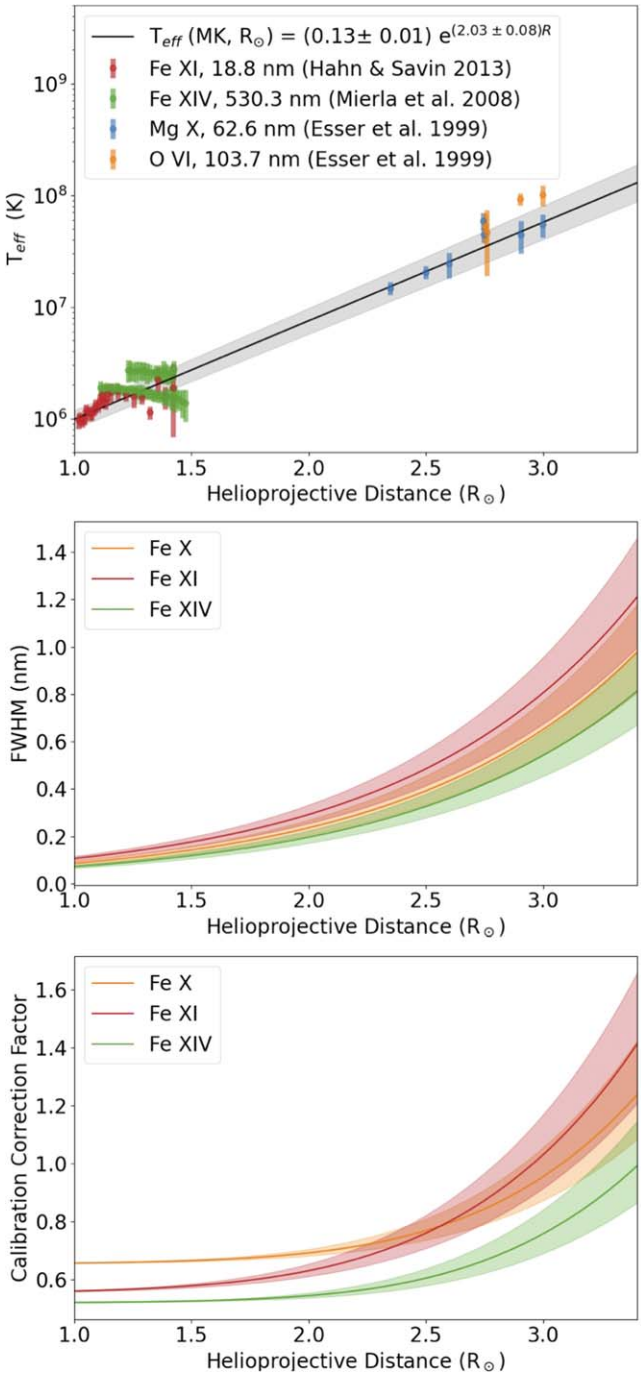

Figure 5. Top: effective ion temperature data from various spectral line observations (Esser et al. 1999; Mierla et al. 2008; Hahn & Savin 2013). The best fit of the data is indicated by the black line, with the gray band indicating the uncertainty of the fit. Middle: calculated FWHM for the Fe X, Fe XI, and Fe XIV lines at different helioprojected distances based on the $T_{\rm eff}$ fit. Bottom: the calibration correction factor for each line (C_i, see Equation (2)), given the FWHMs in the middle panel.

converts the $B_\odot$ unit used with the K + F corona into an analogous unit relative to the Gaussian line profiles. That is, the conversion translates the line signal into solar disk brightness units integrated over the Gaussian line profile.

As expected, in regions where the line widths are substantially smaller than the bandpass, this correction approached the limit where the line is a delta function at the center of the bandpass. As the line grows in width, it started to cover regions of the bandpass where the transmission is lower, and so the relative transmission of the line changes. Only in the outer corona beyond about 2 $R_\odot$ does the increasing line width start to become noticeable in the calibration correction. The rather small changes in the calibration corrections for different FWHM also strengthen the validity of our assumptions, since even rather large changes in the assumed $T_{\rm eff}$ lead to exceptionally small changes in the calibration correction factor. At future TSEs, we intend to deploy slightly larger bandpasses (perhaps 1 nm) to avoid this behavior altogether at larger helioprojective distances.

3. Eclipse Observables

Despite the large abundance of observations of visible and near-infrared coronal line emission via both TSE and coronagraphs, this work is the first to quantify the absolute brightness of Fe X, Fe XI, and Fe XIV optical emission lines beyond ≈1.7 $R_\odot$ (see Section 1). In Section 3.1, we discuss the spatially resolved brightness values inferred for the various emission lines; in Section 3.2 we use the line ratios between the Fe lines to infer the spatially resolved coronal T_e.

3.1. Absolute Brightness of Fe X, XI, and XIV

The photometrically calibrated line emission data in solar disk brightness units integrated over the Gaussian line profiles (as described in Sections 2.1 and 2.2) are shown in the left panels of Figure 6. They have been sliced into a Cartesian representation of polar coordinates for analysis purposes. This slicing also helps to increase the signal-to-noise ratio (S/N) in the outer corona, since greater coronal projected distances have the signal averaged from more pixels in each bin. The data are only utilized in pixels where S/N > 2 for the photometric data, as determined by the propagation of photometric errors for both the on- and off-band frames. We also overplot contours of powers of 10 of brightness in units of the solar disk brightness.

Although one could convert these brightness values into absolute units by using the solar spectrum irradiance at the wavelength of the given line, here we chose to leave the values in units of solar disk brightness. The main motivation for this choice is that these lines are radiatively excited in the corona by photospheric photons, so the absolute energy irradiated by the ions will be tied to the incoming radiation from the Sun. Since we are interested in studying the physical properties of the corona, it makes more sense to consider the lines relative to the photospheric spectrum to remove any wavelength-dependent effects. Furthermore, to infer the relative ionic abundances (and thus T_e) one must also account for the incident photon flux in the corona, which is achieved through the solar brightness units (see Section 3.2).

The latitudinal differences of the line emission are best illustrated in Figure 7, where we show traces of the line brightnesses at the fixed helioprojective distances of 1.2, 1.5, 2, and 2.5 $R_\odot$. The radial drop-off of the line brightness is most evident in Figure 8, where radial traces of the line emission are shown for a set of latitudinal regions.

It is clear from both Figures 7 and 8 that Fe XI is by far the brightest emission line of the three. In fact, it is the only line that retains high-S/N data until 3.4 $R_\odot$, with a brightness of about $5 \times 10^{-10} B_\odot$. The extent of the Fe XI emission data was limited more by the size of the detector used for the observations than by the strength of the line emission. In the future, we plan to use a wider field of view with a larger

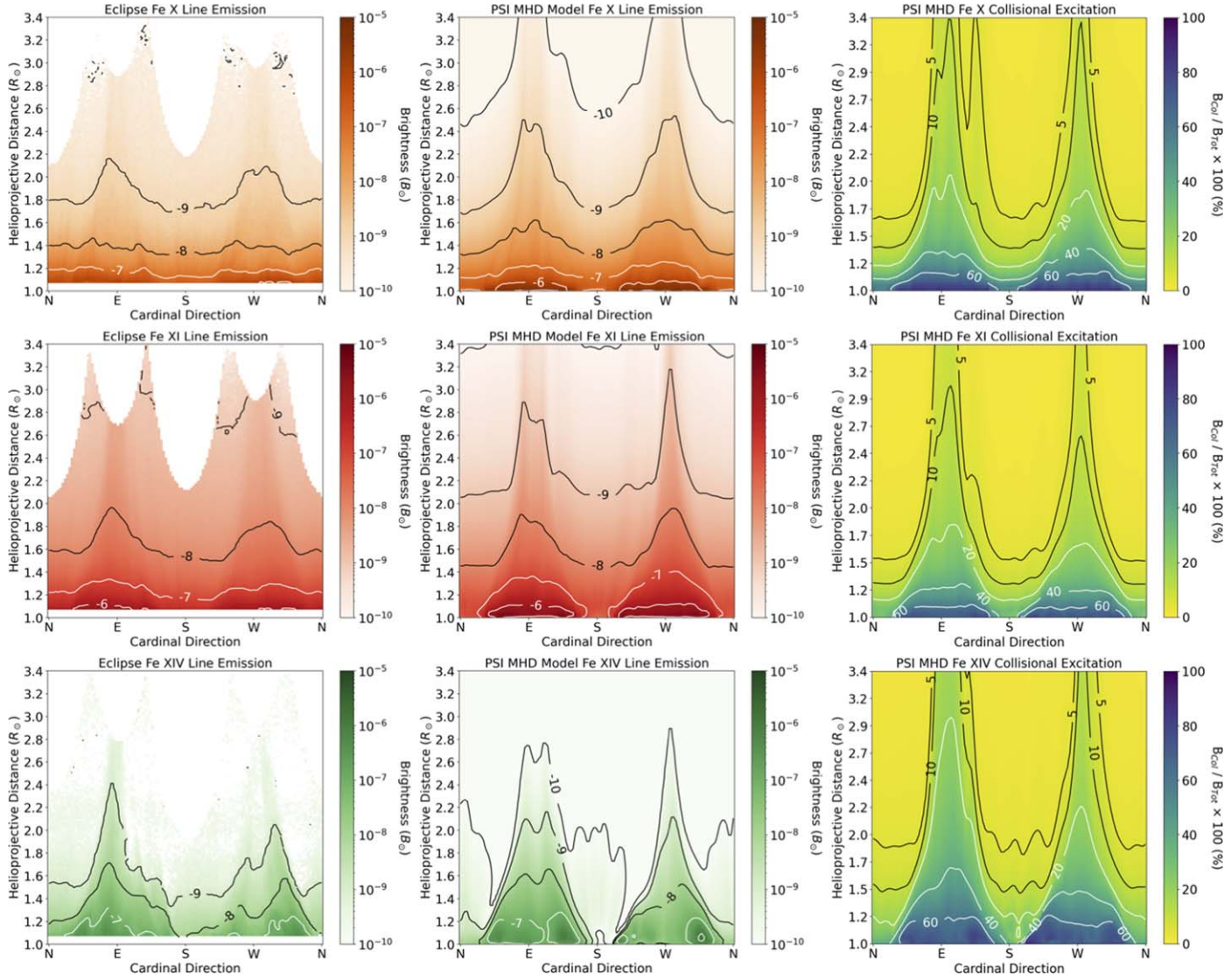

Figure 6. Left panels: calibrated absolute line emission brightness of Fe X, Fe XI, and Fe XIV. The panels are shown in a Cartesian representation of polar coordinates, with contours indicating decades of brightness. Middle panels: same as left but for the PSI MHD prediction of the brightness for each line (see Section 4). Right panels: PSI MHD prediction of the percentage of each line brightness that is caused by collisional excitation.

detector to enable observations of line emission out to even greater helioprojective distances.

In streamers, the brightness of Fe XI ranges from just over $10^{-6}B_\odot$ below 1.2 $R_\odot$, and falls to about $5 \times 10^{-9}B_\odot$ by 3 $R_\odot$. The spatial distribution of Fe XI emission roughly correlates with the K-corona (electron scattering) emission inferred for this eclipse (see Boe et al. 2021a). The K-corona is two to three times brighter than Fe XI throughout the corona, but the line brightness drops to only a small fraction (about 10%) of the total continuum K + F corona brightness beyond about 2 $R_\odot$.

The Fe X emission behaves somewhat similarly to Fe XI, albeit with a considerably lower brightness. It reaches only about $5 \times 10^{-7}B_\odot$ below 1.2 $R_\odot$, and fades to about $10^{-10}B_\odot$ by 3 $R_\odot$. The Fe X emission also has a much less pronounced variation with solar latitude, especially at distances less than ≈1.5 $R_\odot$, where the brightness of the streamers and coronal holes is comparable. Beyond 1.5 $R_\odot$, on the other hand, the brightness variation of Fe X looks much more similar to Fe XI shifted down by an order of magnitude.

By contrast, the Fe XIV emission shows the largest difference between coronal holes and streamers, with fine-scale variations throughout the streamers. It is almost as bright as Fe XI in the core of streamers below 1.5 $R_\odot$, but fades very quickly at greater elongations. Indeed, Fe XIV is the only Fe line that is virtually undetectable above the noise in some regions as low as 2 $R_\odot$, while maintaining a higher brightness in streamers out to as much as 2.8 $R_\odot$. Since Fe XIV emission originates from higher-temperature plasmas ($T_e > 1.5$ MK, see Figure 3), the brightness variation implies a very low proportion of high-temperature plasmas at the poles of the Sun and outside the cores of streamers.

3.2. Electron Temperature

The absolutely calibrated Fe line emission from all three lines enables the inference of the density-weighted average T_e for each LOS in the corona by comparing their relative brightness under the assumption of photoexcitation alone. These optical emission lines do have a component of collisional excitation in the low corona below ≈1.2 $R_\odot$, as shown analytically by Habbal et al. (2007), and for this eclipse specifically via the PSI MHD model (see Section 4 and

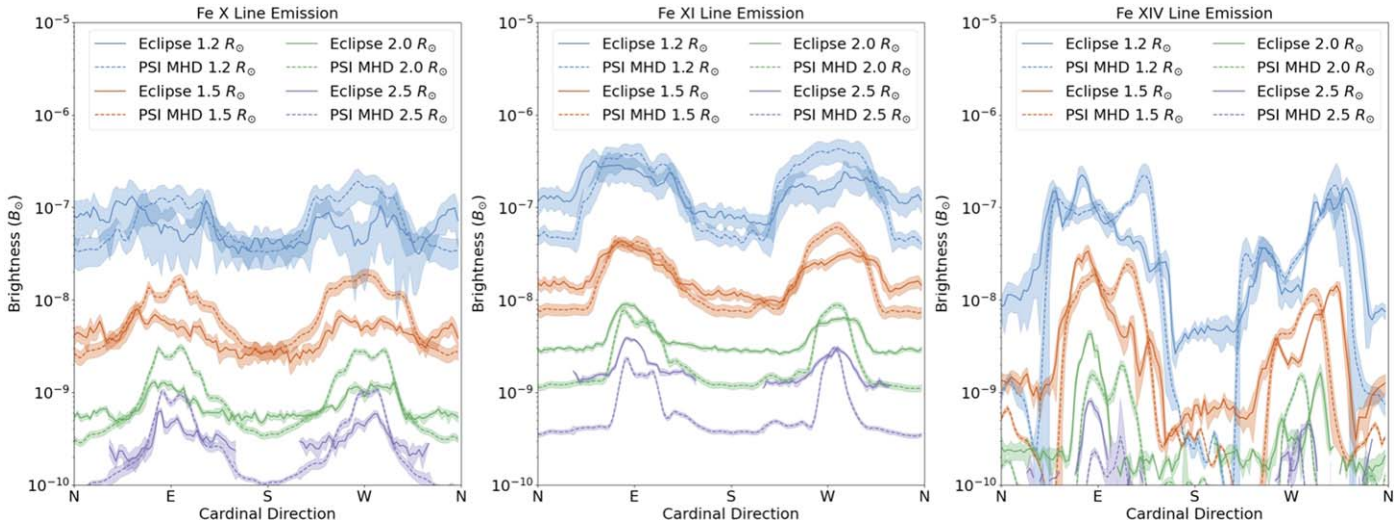

Figure 7. Latitudinal traces of the brightness of Fe X (left), Fe XI (middle), and Fe XIV (right) from the eclipse data (solid lines) and the PSI MHD model (dashed lines). The traces are taken as the median average at fixed helioprojective distances of 1.2 $R_\odot$ (blue), 1.5 $R_\odot$ (orange), 2 $R_\odot$ (green), and 2.5 $R_\odot$ (purple), within 0.1 $R_\odot$ of each distance. The filled region indicates the 1σ scatter of the data points used in the trace.

Figure 6). To correct for the collisional emission, we multiply each emission line by the fractional amount of light that is expected to be from radiative excitation alone (from the MHD model). Since we will use the line ratio to infer T_e, this correction is somewhat independent of the exact density in the model and rather corrects for the relative intrinsic sensitivity that the specific emission line has to collisions.

Here we apply the methodology of Boe et al. (2020a), who used the calibrated ratio of Fe XIV/Fe XI from data acquired at multiple sites during the 2017 TSE, and expand it to line ratios including Fe X.

A given ionic abundance ratio (n_j/n_k) can be related to the intensity ratio of line emission I, for two lines j and k as in the following equation:

$$\frac{n_j}{n_k} = \frac{I_j \rho(\nu_k) \epsilon_k A_k g_{l,j} g_{u,k} {\nu_k}^3}{I_k \rho(\nu_j) \epsilon_j A_j g_{u,j} g_{l,k} {\nu_j}^3}, \quad (3)$$

where the A values are the Einstein coefficients for spontaneous emission, g_u and g_l are the statistical weights for the higher and lower energy levels of the given transition, ν is the frequency of the light emitted by the transition, the ϵ values indicate the photometric efficiency of the telescope systems (and Earth's atmosphere), and the $\rho(\nu)$ terms are the volumetric photon energy density in the corona where the ions are being excited. The A, g, and ν constants used for this work are shown in Table 1.

Equation (3) can be simplified since the product $\rho(\nu)\epsilon$ for each line is accounted for in the absolute photometric calibration of the line brightness into solar disk brightness units (see Section 3.1). The $\rho(\nu)$ terms are technically composed of the solar spectral energy distribution (accounted for via the solar disk brightness unit) and the volumetric scattering geometry of the corona and extended solar disk. However, these volumetric considerations will be identical for any two lines integrated over the same LOS, hence they disappear in a line ratio. Equation (3) then reduces to

$$\frac{n_j}{n_k} = \frac{\beta_j A_k g_{l,j} g_{u,k} {\nu_k}^3}{\beta_k A_j g_{u,j} g_{l,k} {\nu_j}^3}, \quad (4)$$

where the β terms refer to the brightness of the emission lines in units of the solar disk brightness, rather than the absolute intensity of the lines (so $\beta_i = I_i \rho(\nu_i)^{-1} \epsilon_i^{-1}$).

Next, we convert the ionic density ratio from Equation (4) to an inference of T_e based on the ionic abundances as a function of T_e from CHIANTI (see Section 2 and Figure 3). With the Fe X, Fe XI, and Fe XIV observations, we calculate three different line-ratio temperatures for each possible combination. The resulting ionic density ratios and T_e maps are shown in Figure 9. We only display pixels where S/N > 2 for both lines used in each line ratio based T_e inference. These panels are shown out to a heliocentric distance of 2.8 $R_\odot$, rather than 3.4 $R_\odot$ as in Figure 6. The shorter distance was used for this figure because the signal of the Fe XIV line specifically was exceptionally weak beyond this distance, and so the inferred line ratios would not be robust for distances beyond 2.8 $R_\odot$.

We find that Fe^{10+} (Fe XI) is the most abundant ion throughout the corona, even in higher-T_e regions. Fe^{9+} (Fe X) is comparable to Fe^{10+} in the low corona below 1.3 $R_\odot$, but is 3–5 times less abundant beyond that distance. Fe^{10+} is always more abundant than Fe^{13+} (Fe XIV) everywhere in the corona. In fact, Fe^{13+} is never more than ≈50% as abundant as Fe 10^+, even in the hottest regions at the core of the eastern streamer. Nevertheless, Fe^{13+} is up to twice as abundant as Fe^{9+} in the high-T_e regions. The Fe^{13+} abundance drops dramatically in open field regions, however, often to less than 10% of the abundance of Fe^{9+}. The result that Fe^{10+} is the most abundant ion in the corona supports Habbal et al. (2010b, 2021), who found it to be the most abundant Fe ion in the solar wind, and it is the brightest Fe emission line in the corona, regardless of solar cycle.

The T_e values inferred from the Fe XIV/Fe XI and Fe XIV/Fe X line ratios are consistent with each other, as demonstrated by the direct comparison between these T_e inferences for each LOS in the top left panel of Figure 10. The T_e inferred from Fe XIV/Fe X is only 2.5% higher than the Fe XIV/Fe XI T_e value on average. The rms variance of the average is 3.7%, so the two methods are statistically equivalent. Both inferences range from about 1.25 to 1.4 MK in the coronal holes and about 1.5 to 1.65 MK in the equatorial streamers. The streamers show

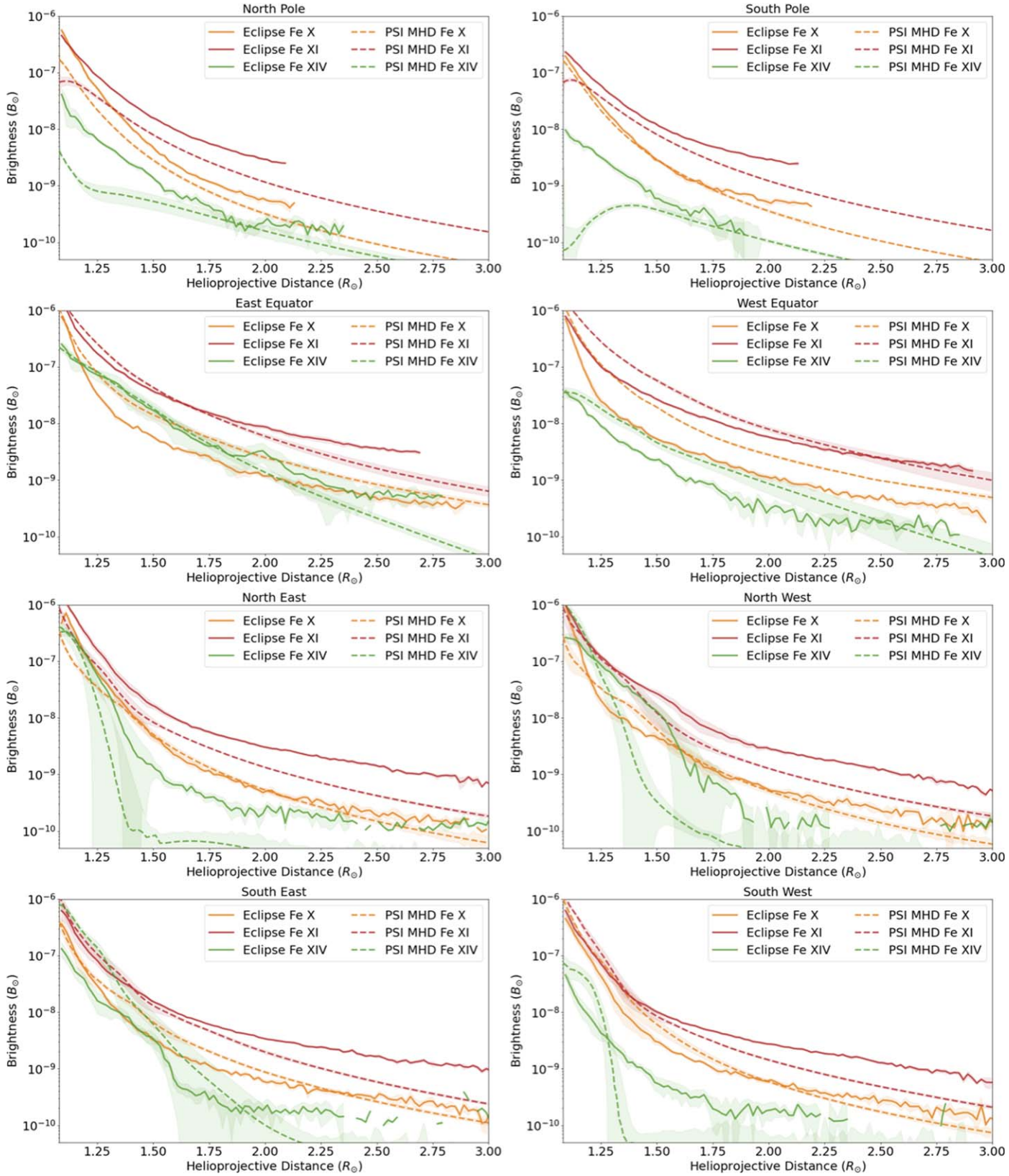

Figure 8. Radial traces of the brightness of Fe X (orange), Fe XI (red), and Fe XIV (green) from the eclipse data (solid lines) and the PSI MHD model (dashed lines). The traces are taken from the median average inside a 15° wedge centered on the cardinal direction indicated in the title of each panel. The filled bands show the 1σ scatter of data points within the wedge.

a large spatial variability of T_e where the streamer cores are hotter (about 1.6 MK) than the boundaries (1.5 MK). There are also pockets of lower-temperature plasmas (1.3 MK) at the base of the streamers below 1.2 $R_\odot$. The thickness of the streamers (as visualized by the spatial distribution of T_e) also decreases at larger helioprojective distances, while the coronal

Table 1
Constants Used for Equation (4)

Line	λ_{ion} (nm)	ν_{ion} (10^{14} Hz)	A_{ion} (s^{-1})	g_l	g_u
Fe X	637.5	4.70	69.4	4	2
Fe XI	789.2	3.80	43.7	5	3
Fe XIV	530.3	5.65	60.2	2	4

Note. Data are from NIST (Kramida et al. 2021 and references therein).

holes dominate more of the corona with a roughly uniform temperature.

T_e inferred from Fe XI/Fe X is quite different from T_e inferred from the two line ratios involving Fe XIV, where a much larger range of temperatures is inferred. This line ratio indicates that the coronal hole T_e is closer to 1.1 MK with distinct fine-scale plumes of cool plasma emerging into the corona. The core of the streamers then is over 1.8 MK in this inference, while the outer corona is quite a bit higher in temperature than the other line ratio inferences. While the Fe XI/Fe X ratio provides an interesting map for showcasing small temperature variations in the coronal hole plumes, it is not a very reliable measure of the temperature. One reason for this large spread of T_e is that the slope of the Fe XI/Fe X ionic abundance ratio as a function of T_e is considerably shallower than that of the other line ratios (see Figure 4). Therefore, a small change in the emission ratio leads to a large change in the inferred temperature. The range of temperature response of the Fe X and Fe XI curves alone also does not probe the range above about 1.5 MK effectively; consequently this line ratio is unreliable anywhere outside the coolest regions in the corona. The large difference in T_e inferred from Fe XI/Fe X and from the other line ratios perhaps implies that the corona is not isothermal along a single LOS, and so the LOS average is not identical for different line ratio inferences. Additionally, average T_e inferences from two line ratios may be biased toward finding temperatures in-between the peak ionization of the temperature response functions (i.e., Figure 4) as demonstrated in the EUV by Weber et al. (2005). We intend to explore a more complex T_e inference using all three (or more) of these visible emission lines simultaneously in a future study, as it is beyond the scope of this work.

4. The PSI MHD Model

The spatially resolved coronal line emission (Figure 6) and inferred electron temperature (Figure 9) are the first such data to span the distance of 1.08 to 2.8 $R_\odot$ (up to 3.4 $R_\odot$ for Fe XI), and offer a unique opportunity to test and constrain advanced models of the corona. Specifically, we compare our observational eclipse results to forward-modeled line emission using the state-of-the-art MHD simulation of the PSI model (Mikić et al. 2018) for the corona in the 2019 July 2 total solar eclipse.[6] There exists a rich heritage of forward-modeling white-light and EUV observables from the PSI MHD model (e.g., Mikić et al. 1999; Mok et al. 2005; Lionello et al. 2009), where the local emissivity for a given observable (based on the local plasma state and/or geometry) was obtained and then integrated along a given LOS through the model. We follow a similar approach to model the Fe X, Fe XI, and Fe XIV emission lines (see Section 4.1).

[6] http://www.predsci.com/corona/jul2019eclipse/home.php

This MHD model was used by Boe et al. (2021a), where the forward-modeled K-corona emission (top right panel of Figure 1) was compared to the eclipse data (see Boe et al. 2021a for the details of the model). The model was found to accurately predict the brightness of the K-corona, and consequently the electron density. Further, the magnetic morphology of the model (bottom right panel of Figure 1) closely matches the fine-scale striations seen in the eclipse image. Given that the MHD model has generated a reasonable prediction of electron density and magnetic field morphology throughout the corona, we can reliably extend the comparison to include the line emission observables, which offers a unique opportunity to test other plasma parameters in the model.

4.1. Forward-modeled Line Emission

Assuming local thermodynamic equilibrium, the total line emissivity of a parcel of plasma depends on the local electron density, temperature, and radiation field near the line center, originating from both radiative and collisional excitation. To tackle this problem, we use the CHIANTI 10 database and software package (as described in Section 2) and its framework for adding photoexcitation to the calculations of level populations (Young et al. 2003). The contribution function for each Fe line individually is computed on a 3D grid of density, temperature, and solar radius. The radial distance is then used to approximate the local radiation field at these wavelengths by using the observed solar spectral irradiance from the International Space Station (Meftah et al. 2018). This lookup table for the contribution function is then used to calculate the local emissivity at each point along the LOS in the forward-modeling computation.

For the abundance factor we adopt the "hybrid" coronal abundances (Schmelz et al. 2012), which match the radiative loss function used in the thermodynamic MHD calculation. We can also turn off the photoexcitation flags in the CHIANTI calculation to compute contribution functions based on collisions alone and use these in a separate forward-modeling experiment. This enables us to compare the relative importance of collisional excitation for each LOS in the forward-modeled line emission. Finally, to compare the model calculations with the eclipse observations, we convert the LOS-integrated emission into solar disk brightness units by using the solar spectral irradiance and accounting for the angular size of the solar disk, which had a radius of about 943″ at the time of the eclipse (Earth was at aphelion).

Radially flattened versions of the model-predicted Fe X, Fe XI, and Fe XIV line emission are shown in the bottom panels of Figure 2. The photometric brightness predictions of all three lines are shown in the middle panels beside the observed emission in Figure 6, with the same Cartesian representation of polar coordinates as the eclipse data in the left panels. In the right panels of the figure, we show the percentage of the emission that originates from collisional excitation compared to the total brightness of each line. Collisional excitation is important in the low corona inside streamers, but the photoexcitation becomes the dominant excitation process everywhere beyond 1.2 $R_\odot$. We use the modeled fraction of emission that is radiative to correct the emission observations specifically for the T_e values inferred from the line ratio (as done in Section 3.2). However, it is possible that our T_e inferences are not as robust at the base of streamers. This region is commonly explored through EUV observations, since

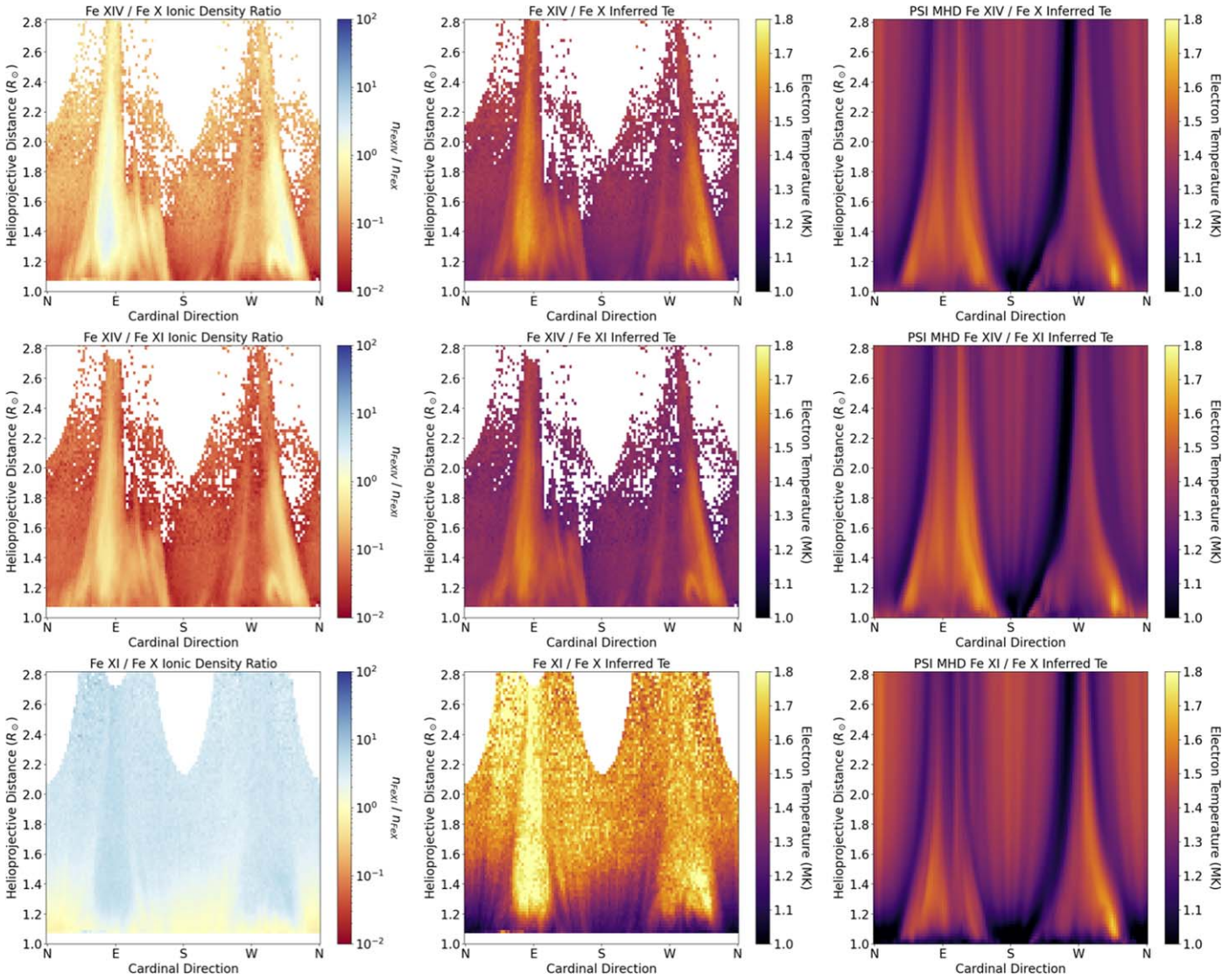

Figure 9. Left panels: ionic density ratios inferred from the line ratios of Fe XIV/Fe X (top), Fe XIV/Fe XI (middle), and Fe XI/Fe X (bottom) using Equation (4) and the observed line brightnesses. Middle panels: inferred T_e from the ionic density ratios to the left, using the curves of ionization ratio shown in Figure 4. Right panels: inferred T_e using the predicted line emission from the PSI MHD model (see Section 4).

EUV emission is predominantly collisionally excited, so it is not crucial for these eclipse observations to robustly probe the collisionally dominated regions of the corona. Nevertheless, our T_e results are generally consistent with the values inferred via EUV observations during periods close to solar minimum (e.g., Morgan & Taroyan 2017).

4.2. Testing the Model

4.2.1. Line Emission Comparisons

While the PSI MHD model generally makes reasonably accurate predictions of the overall brightness and structure of coronal line emission as inferred from the eclipse data, there are some notable differences. These differences are best seen in Figures 7 and 8, in the comparison of the latitudinal and radial traces of the line emission from both the eclipse data and the model.

The prediction of Fe X is the best overall. For this line, the model and data are an excellent match below about 1.5 $R_\odot$, and disagree only slightly for larger elongations. At the greater distances the model brightness is too high in the streamers by about a factor of 2. In the eclipse data, the Fe X line emission is more uniform throughout the corona than is predicted by the model regardless of the coronal structures.

The prediction of Fe XI is also quite good, especially in the streamers. However, the model significantly underestimates the Fe XI emission in the coronal holes, and the difference grows for larger helioprojective distances. This difference in coronal holes is an indication that the model is underestimating the density of Fe XI in the outflowing solar wind.

The Fe XIV line is more complex to compare, in large part because the line is sensitive to the higher-temperature regions in the corona that are controlled by complex dynamics in the closed-field regions of streamers and active regions. Indeed, the precise brightness differences on small spatial scales between the model and observations for Fe XIV specifically are not always meaningful, since small variations are easily caused by slight errors in the angle of streamers in the model, which can be tilted by quite small changes in the polar magnetic fields used in the model (Riley et al. 2019). For Fe XIV it is then not

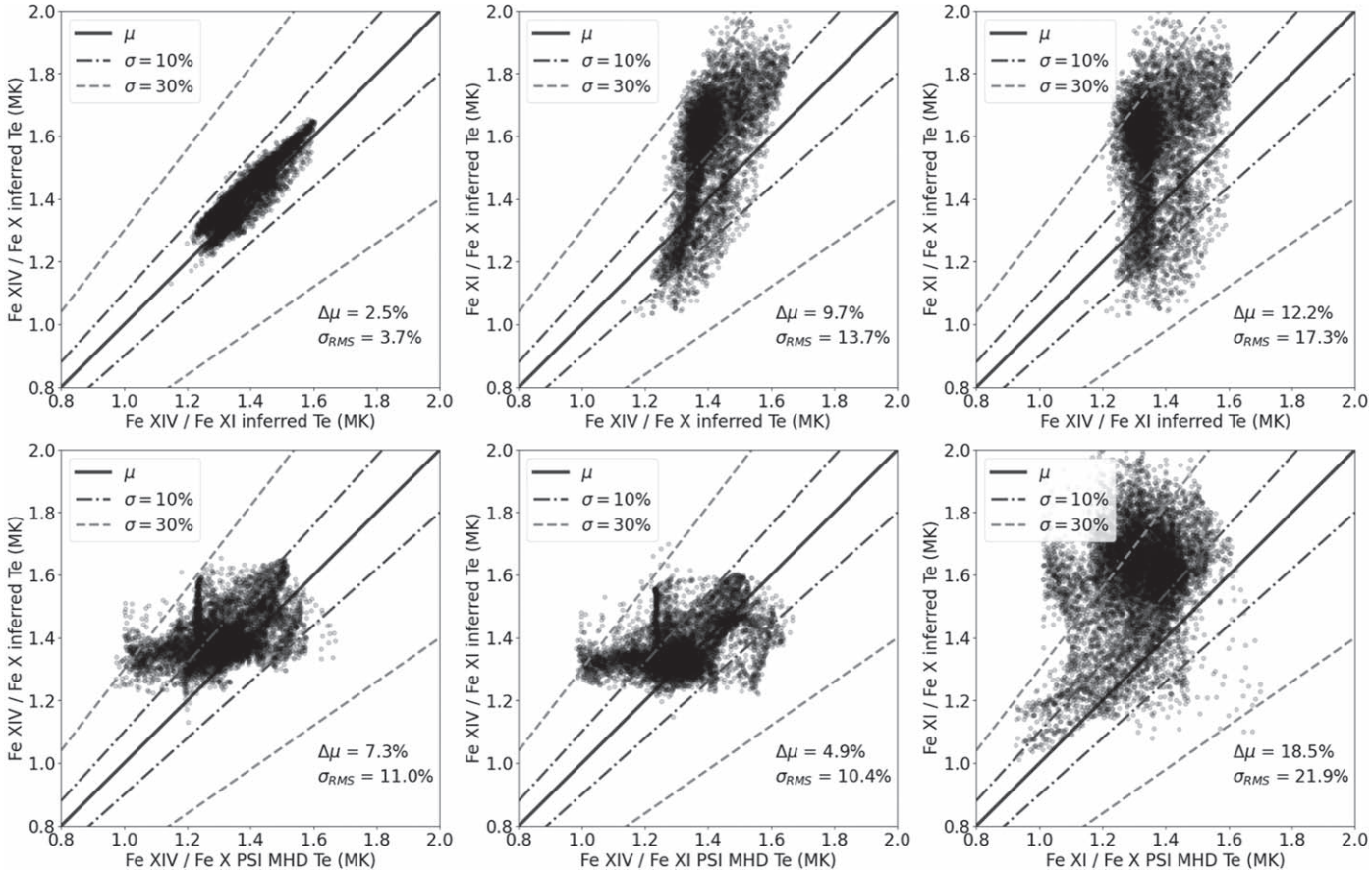

Figure 10. Comparative scatter plots of the electron temperature from the Fe XIV/Fe X, Fe XIV/Fe XI, and Fe XI/Fe X line ratios (see Section 3.2), along with the PSI MHD prediction-driven inferences from the same line ratios (see Section 4). The solid line shows the 1:1 correspondence, and the dotted–dashed (dashed) lines show a ±10% (±30%) variance from the 1:1 correspondence. The mean offset is written as $\Delta\mu$ with the sign indicating whether the average is above or below the 1:1 line, and $\sigma_{\rm RMS}$ indicates the rms variance of the data points around the mean offset.

useful to compare each individual LOS between the model and the eclipse data necessarily, but rather to compare the general trends and range of values seen from different coronal structures at various elongations. Still, the overall PSI MHD prediction of Fe XIV is reasonably close for streamer regions, but has some large differences in the coronal holes, where the model substantially underestimates the brightness—in a similar manner to the Fe XI prediction.

4.2.2. *Inferred* T_e *Comparisons*

Next, we use the model line emission of the Fe lines to infer T_e, replicating the approach used with the eclipse data (see Section 3.2). We use the inferred T_e from the model line emission rather than the actual T_e in the model since the resulting inference will be systematically the same as the eclipse inference. The comparison between these inferences is a more direct test of the modeled temperature and density distributions, because it uses the emission line observables directly (and thus the formation mechanism, density, and temperature along the LOS) as opposed to comparing directly to the plasma temperature in the model.

The PSI MHD model predictions of T_e from the Fe XIV/Fe XI, Fe XIV/Fe X, and Fe XI/Fe X model line ratios are shown in the right panels of Figure 9. The eclipse and model inferences for each LOS are compared in Figure 10. Although the model predictions show similar qualitative structures to the eclipse inferred T_e maps, the model inferences are slightly lower on average. However, the spread of T_e between the eclipse and model inferences indicates that the global average T_e of the model inferences is rather similar to the eclipse inference. Specifically the Fe XIV/Fe X inference is $7.3\% \pm 11.0\%$ lower, and the Fe XIV/Fe XI inference is $4.9\% \pm 10.4\%$ lower than the eclipse inference.

As discussed in Section 3.2 the Fe XI/Fe X line ratio is a somewhat unreliable measurement of the higher temperatures in the corona. It is then not surprising that the model and the eclipse inferences diverge for this line ratio T_e for temperatures higher than about 1.4 MK, although the model and the data match reasonably well for the lower temperatures.

These comparisons illustrate some of the ways in which these unique observables can be used to test and validate coronal models in the low to middle corona. The relative agreement of the model and observations in the closed-field regions suggests that it is doing a reasonably good job at reproducing both the electron density and temperature distributions there, which are set by the interplay of the 3D closed magnetic field geometries and the coronal heating model. Nevertheless, the model somewhat overestimates the Fe X brightness in the streamers beyond 1.2 $R_\odot$, suggesting it may be slightly underestimating T_e in the outer regions of streamers.

Further, the model underestimates Fe XI and Fe XIV in the polar coronal holes, which is particularly interesting from the perspective of constraining future models. Perhaps the simplest

explanation would be that the current model is underestimating the density profiles within the coronal holes. However, the K-corona analysis of Boe et al. (2021a) for this eclipse found that the model had a virtually identical K-corona brightness to that inferred from observations, and the K-corona brightness depends only on the 3D electron density distribution. Ruling out density, the next possibility would be a temperature effect, i.e., the model is underpredicting the average T_e in this region or below, which would shift the Fe charge state distribution away from Fe XI and Fe XIV.

A temperature disagreement, in turn, could imply a deficiency in the coronal heating formalism in the MHD model, which in this case is set by a wave-turbulence-driven approach (Lionello et al. 2014; Downs et al. 2016; Mikić et al. 2018). On the other hand, the independent density constraint set by the K-corona observables suggests that simply increasing heating to raise the coronal temperature may not be a viable solution, as this will greatly influence the density distribution along the flux tube as well. Instead, this may point to an issue with the distribution of heating along open flux tubes in the low corona or in the complexity of the equations solved, such as solving for a single temperature (as is done here) or using a multi-temperature and/or fluid approximation (e.g., van der Holst et al. 2022).

This analysis is also complicated by the fact that charge-state freeze-in is likely to have occurred relatively low in the corona (roughly 1.2–2 $R_\odot$), as supported by our analysis for the 2015 total solar eclipse (Boe et al. 2018) and by empirical modeling (Gilly & Cranmer 2020). Considering that the frozen-in charge state distributions are sensitive to the temperature, density, and velocity distributions where freeze-in occurs (e.g., Lionello et al. 2019), the combination of broadband K-corona (density) and photoexcited emission lines (charge states) can provide tight constraints on coronal and solar wind models. We will explore improvements to the MHD model and the role of nonequilibrium ionization on the forward-modeled observables in a future study.

5. Conclusions

The 2019 total solar eclipse was an excellent example of a solar minimum corona and so presented a unique opportunity to study the properties of a relatively quiescent corona. In this work, we expanded on the continuum data set of Boe et al. (2021a) by analyzing the line emission observations of Fe X, Fe XI, and Fe XIV, which corresponded to the continuum bandpasses in that paper (see Section 2). We have presented absolutely calibrated (in units of solar disk brightness) spatially resolved line emission for these lines from 1.08 up to as much as 3.4 $R_\odot$ for the first time (see Section 3.1). This unique combination of broadband and narrowband line observables provides strong constraints for the model and the distribution of heating as a function of height. Such constraints can be used to improve our understanding of the physics of coronal holes and the nascent solar wind.

Equipped with the calibrated line emission, we inferred the electron temperature (T_e) using two-line ratios between each pair of Fe lines (see Section 3.2). We find that:

1. The Fe^{10+} ion is the most abundant of the three throughout the corona, supporting the work of Habbal et al. (2010b, 2021).
2. The Fe XIV/Fe X and Fe XIV/Fe XI line ratios produce effectively the same T_e with the streamers having a temperature of about 1.65 MK at the core, and closer to 1.5 MK at their border, whereas the coronal holes are at about 1.25 to 1.4 MK.
3. The streamers have pockets of lower T_e plasmas at their base from 1.08 to 1.3 $R_\odot$, but have significantly higher T_e in their cores at greater helioprojective distances.
4. The width of the streamers, as inferred from the T_e distribution, reduces substantially with distance from the Sun while the rest of the corona is almost isothermal everywhere beyond 1.2 $R_\odot$ or so.

We then compared our line emission and T_e results to the MHD model from Predictive Science Inc. The forward-modeled line emission matches the eclipse observations reasonably well in the closed-field streamer regions, although it slightly underestimates the Fe X brightness there. The model likewise underestimates the brightness of Fe XI and Fe XIV in the polar coronal holes. In Boe et al. (2021a), the K corona of the same PSI MHD model was compared to the eclipse data, and was found to be an excellent match, implying that the differences between the eclipse and model line emission are not due to a density effect. Instead, these differences are most likely due to a slightly too low energization of the coronal plasma in the model, especially in the polar coronal holes. There could also be a freeze-in/nonequilibrium effect that is shaping the ion distributions in a nontrivial manner (see Section 4.2.2). We intend to explore the exact relationship of the inferred temperatures to the underlying plasma state and the implied systematics in another paper, as it is beyond the scope of the work presented here.

Another important finding of this work is that Fe XI emission is clearly detectable out to at least 3.4 $R_\odot$ with relatively small telescopes and only a couple of minutes of observing time—at an eclipse that was near solar minimum where the coronal density (and thus brightness) is at its lowest. It is therefore likely that one could observe line emission to an even greater helioprojective distance at eclipses. We intend to deploy instruments with wider fields of view in the future to expand on the maximum distance at which line emission can be measured. Further, this finding suggests that space-based coronagraphs that have rather large occulters ($\approx$2 $R_\odot$) could be used to measure line emission. Any stray light contamination would be accounted for by subtracting the continuum with an off-band filter as well (see Section 2), since the stray light would be effectively the same over a small wavelength shift between the on- and off-band filters.

This work also strengthens the value of the forthcoming line emission observations from the ground-based UCoMP instrument (Tomczyk et al. 2021), which can perform similar analysis to that done here, but with a much longer time baseline. While the ground-based observations cannot probe to as great a helioprojective distance due to the sky brightness of the Earth, they could still explore the line emission and T_e time variations in the corona—as Boe et al. (2020a) demonstrated for multiple observing sites spaced out over the United States during the 2017 TSE with similar instrumentation to that used in this work. The calibration and line width corrections made here (see Section 2.2) can offer a means to measure the absolute brightness (and T_e) of additional lines with UCoMP in the near future.

Finally, as planned manned lunar missions ramp up in the next decade or so, it may be possible to use the Earth as an occulter during lunar eclipses (i.e., a total solar eclipse on the Moon) or to use the Moon as an occulter while in lunar orbit as proposed by Habbal et al. (2013). The extent of line emission here implies that despite the large size of the Earth, such data would be useful for achieving long exposures of line emission in the corona. As the Earth moves from one side of the corona to the other, the observations could focus on the opposite side of the corona for half of the eclipse duration (which is hours on the Moon, compared to minutes on the Earth). Rather small payloads, similar to the ones used here, could be deployed to the lunar surface or to orbiters such as the planned Lunar Gateway station to take advantage of the multiple lunar eclipses that occur every year.

We thank Judd Johnson and Pavel Štarha, who acquired the narrowband data at the Rodeo, Argentina, observing site during the 2019 July 2 total solar eclipse.

The K-Cor data were courtesy of the Mauna Loa Solar Observatory, operated by the High Altitude Observatory, as part of the National Center for Atmospheric Research (NCAR). NCAR is supported by the National Science Foundation.

Observables presented in this paper and other eclipse data from our group can be found at: https://www.ifa.hawaii.edu/SolarEclipseData/. The PSI MHD model eclipse predictions can be found here: https://www.predsci.com/corona/.

Financial support was provided to B.B. by the National Science Foundation under Award No. 2028173. S.H. and the 2019 eclipse expedition were supported under NASA grant NNX17AH69G and NSF grant AST-1733542 to the Institute for Astronomy of the University of Hawaii. C.D. was supported by the NASA Heliophysics Supporting Research and Living With a Star programs (grants 80NSSC18K1129 and 80NSSC20K0192). M.D. was supported by the Grant Agency of Brno University of Technology, project No. FSI-S-20-6187.

ORCID iDs

Benjamin Boe https://orcid.org/0000-0002-6396-8209
Shadia Habbal https://orcid.org/0000-0003-4089-9316
Cooper Downs https://orcid.org/0000-0003-1759-4354

References

Agrawal, D. C. 2016, EJPh, 37, 035601
Altrock, R. C. 2011, SoPh, 274, 251
Bessey, R. J., & Liebenberg, D. H. 1984, SoPh, 94, 239
Boe, B., Habbal, S., Downs, C., & Druckmüller, M. 2021a, ApJ, 912, 44
Boe, B., Habbal, S., Druckmüller, M., et al. 2018, ApJ, 859, 155
Boe, B., Habbal, S., Druckmüller, M., et al. 2020a, ApJ, 888, 100
Boe, B., Habbal, S., & Druckmüller, M. 2020b, ApJ, 895, 123
Boe, B., Yamashiro, B., Druckmüller, M., & Habbal, S. 2020c, ApJL, 914, L39
Chandrasekhar, T., Ashok, N. M., Desai, J. N., Pasachoff, J. M., & Sivaraman, K. R. 1984, ApOpt, 23, 508
Del Zanna, G., & DeLuca, E. E. 2018, ApJ, 852, 52
Del Zanna, G., Dere, K. P., Young, P. R., & Landi, E. 2021, ApJ, 909, 38
Dere, K. P., Landi, E., Mason, H. E., Monsignori Fossi, B. C., & Young, P. R. 1997, A&AS, 125, 149
Dima, G. I., Kuhn, J. R., & Schad, T. A. 2019, ApJ, 877, 144
Ding, A., & Habbal, S. R. 2017, ApJL, 842, L7
Downs, C., Lionello, R., Mikić, Z., Linker, J. A., & Velli, M. 2016, ApJ, 832, 180
Druckmüller, M., Rušin, V., & Minarovjech, M. 2006, CoSka, 36, 131
Esser, R., Fineschi, S., Dobrzycka, D., et al. 1999, ApJL, 510, L63
Gilly, C. R., & Cranmer, S. R. 2020, ApJ, 901, 150
Guhathakurta, M., Rottman, G. J., Fisher, R. R., Orrall, F. Q., & Altrock, R. C. 1992, ApJ, 388, 633
Habbal, S. R., Druckmüller, M., Alzate, N., et al. 2021, ApJL, 911, L4
Habbal, S. R., Druckmüller, M., Morgan, H., et al. 2010a, ApJ, 719, 1362
Habbal, S. R., Morgan, H., Druckmüller, M., & Ding, A. 2010b, ApJL, 711, L75
Habbal, S. R., Morgan, H., Druckmüller, M., et al. 2013, SoPh, 285, 9
Habbal, S. R., Morgan, H., & Druckmüller, M. 2014, ApJ, 793, 119
Habbal, S. R., Morgan, H., Johnson, J., et al. 2007, ApJ, 663, 598
Hahn, M., & Savin, D. W. 2013, ApJ, 776, 78
Koutchmy, S., Baudin, F., Abdi, S., Golub, L., & Sèvre, F. 2019, A&A, 632, A86
Kramida, A., Yu, R., Reader, J. & and NIST ASD Team 2021, NIST Atomic Spectra Database (ver. 5.9), National Institute of Standards and Technology, Gaithersburg, MD, doi:10.18434/T4W30F, https://physics.nist.gov/asd
Lionello, R., Downs, C., Linker, J. A., et al. 2019, SoPh, 294, 13
Lionello, R., Linker, J. A., & Mikić, Z. 2009, ApJ, 690, 902
Lionello, R., Velli, M., Downs, C., et al. 2014, ApJ, 784, 120
Lyot, B. 1932, ZAp, 5, 73
Lyot, B. 1939, MNRAS, 99, 580
Magnant-Crifo, F. 1973, SoPh, 31, 91
Meftah, M., Damé, L., Bolsée, D., et al. 2018, A&A, 611, A1
Mierla, M., Schwenn, R., Teriaca, L., Stenborg, G., & Podlipnik, B. 2008, A&A, 480, 509
Mikić, Z., Downs, C., Linker, J. A., et al. 2018, NatAs, 2, 913
Mikić, Z., Linker, J. A., Schnack, D. D., Lionello, R., & Tarditi, A. 1999, PhPl, 6, 2217
Mok, Y., Mikić, Z., Lionello, R., & Linker, J. A. 2005, ApJ, 621, 1098
Morgan, H., & Taroyan, Y. 2017, SciA, 3, e1602056
Riley, P., Linker, J. A., Mikic, Z., et al. 2019, ApJ, 884, 18
Rumińska, A., Bak-Stęślicka, U., Gibson, S. E., & Fan, Y. 2022, ApJ, 926, 146
Rybansky, M., Rusin, V., Gaspar, P., & Altrock, R. C. 1994, SoPh, 152, 487
Samra, J. E., Judge, P. G., DeLuca, E. E., & Hannigan, J. W. 2018, ApJL, 856, L29
Schmelz, J. T., Reames, D. V., von Steiger, R., & Basu, S. 2012, ApJ, 755, 33
Singh, J., Saxena, A. K., & Bappu, M. K. V. 1982, JApA, 3, 249
Srivastava, N., Schwenn, R., Inhester, B., Martin, S. F., & Hanaoka, Y. 2000, ApJ, 534, 468
Tomczyk, S., Landi, E., Berkey, B., et al. 2021, AGUFM, 2021, 2089
van der Holst, B., Huang, J., Sachdeva, N., et al. 2022, ApJ, 925, 146
Wang, Y. M., Sheeley, N. R. J., Hawley, S. H., et al. 1997, ApJ, 485, 419
Weber, M. A., Schmelz, J. T., DeLuca, E. E., & Roames, J. K. 2005, ApJL, 635, L101
Young, C. A. 1872, Natur, 7, 28
Young, P. R., Del Zanna, G., Landi, E., et al. 2003, ApJS, 144, 135